Measurement of the Phason Dispersion of Misfit Dislocations on the Au(111) Surface

E. M. McIntosh,[1,*] P. R. Kole,[1] M. El-Batanouny,[2,†] D. M. Chisnall,[1] J. Ellis,[1] and W. Allison[1]

[1]*The Cavendish Laboratory, J. J. Thomson Avenue, Cambridge CB3 0HE, United Kingdom*

[2]*Department of Physics, Boston University, Boston, Massachusetts 02215, USA*

(Received 22 November 2012; revised manuscript received 11 January 2013; published 21 February 2013)

We report measurements of the acoustic and optical phason dispersion curves associated with the lattice of partial dislocations on the reconstructed (111) surface of gold. Our measurements of these low energy (< 0.5 meV) weakly dispersive modes have been enabled by the very high resolution of the novel helium spin-echo technique. The results presented here constitute the first measurement of the phason dispersion of misfit dislocations, and possibly of excitations associated with any type of crystalline dislocations.

DOI: 10.1103/PhysRevLett.110.086103 PACS numbers: 68.35.Ja, 63.20.kp, 68.47.De, 68.49.Bc

The influence of dislocations on the mechanical, electrical, and optical properties of real materials has been widely recognised and has been the subject of extensive research activity [1,2], with the effects of linear and planar dislocations pervading almost every branch of condensed matter physics. Interfaces between dissimilar materials usually suffer from competing length scales (vernier misfit), which in most cases is resolved by the introduction of misfit dislocations, reducing the misfit strain present in the unrelaxed, fully coherent interface. The concept of the misfit dislocation was first introduced by Frenkel and Kontorova [3], applied to orientated monolayer overgrowth by Frank and van der Merwe [4,5], and further developed by Nabarro [6]. Since then there have been numerous observations and characterizations of misfit dislocations in epitaxial thin films [7–9]. The rapidly expanding applications of nano- and microscale devices in many areas of cutting edge technologies have brought the investigation of interfacial dislocations to the fore, since their fabrication involves epitaxial thin film growth processes.

Au(111) is the only close-packed metal surface known to exhibit reconstruction at room temperature [10–14]. Here, a vernier misfit between the surface layer and the underlying bulk gives rise to alternating regions of fcc and hcp stacking which coexist along the $\langle 1\bar{1}0\rangle$ direction, and are separated by a partial misfit (Shockley) dislocation (PMD) described by Burgers vectors of $\mathbf{b}_1 = \frac{1}{6}(\bar{2}, 1, 2)$ and $\mathbf{b}_2 = \frac{1}{6}(1, \bar{2}, 1)$ [15]. Each reconstructed unit cell has a $23 \times \sqrt{3}$ periodicity along the $\langle 1\bar{1}0\rangle$ direction, and contains two PMDs, giving a net one extra atom, and an effective average uniaxial contraction of 4.4% of the surface layer [16]. The additional superstructure, a characteristic herringbone pattern with a domain width of $\sim$150 Å, has been revealed by scanning tunneling microscopy and x-ray diffraction experiments [12–14,17]. The herringbone reconstruction results from the alignment of PMDs along the $\langle 11\bar{2}\rangle$ direction giving rise to stripes of domain or soliton walls marking the transitions between fcc and hcp stacking of the outermost layer, which exhibit regular alternation along two of the possible three $\langle 11\bar{2}\rangle$ orientations.

Here we present the first measurements of the dynamics of misfit dislocations, for the acoustic and optical phason dispersion of PMDs on the Au(111) surface. We use the novel helium spin-echo (HeSE) technique [18], which provides a unique tool for nondestructive measurements of surface dynamical processes occurring at atomic length scales and on pico- to nanosecond time scales. Inelastic helium atom scattering, a long-standing surface technique [19,20], has traditionally employed time of flight methods to study surface dynamics with an energy resolution of ≥ 0.3 meV, which has made it difficult and challenging to separate the instrumental resolution from the dynamical signatures of low-energy physical processes, such as the low energy phason modes studied in this work.

A spin-echo measurement provides a direct measurement of temporal and spatial surface correlations, in the form of an intermediate scattering function (ISF) $I(\Delta\mathbf{K}, t)$, where $\Delta\mathbf{K}$ is the momentum transfer parallel to the surface. Tilting the sample changes the angle of incidence θ_i and hence $\Delta\mathbf{K}$. Here we are concerned with the temporal Fourier transform of the ISF, namely the dynamic structure factor $S(\Delta\mathbf{K}, \omega)$, giving energy loss and gain on scattering of the helium atoms from the sample [18]. For a fixed scattering geometry, here a total scattering angle of $(44.4 \pm 0.1)°$, a single measurement provides a one-dimensional (1D) phonon spectrum. For such measurements, we used a helium-3 beam having an energy of 8.05 meV and a full width half maximum (FWHM) of 0.25 meV.

Two-dimensional (2D) phonon measurements have recently been enabled, where a two-dimensional Fourier transform relationship exists between the measured polarization and the two-dimensional matrix relating the scattered energy to the incident energy [21,22]. For the two-dimensional measurement presented here we used an incident beam having an energy of 8.15 meV and a FWHM of 1.8 meV, together with a sparse sampling technique

that covers $\lesssim 4\%$ of the complete matrix yet provides acceptable accuracy, thus allowing such 2D measurements to be made within practical time scales [23].

The Au(111) surface (SPL, The Netherlands) was cleaned by repeated cycles of sputtering (0.5 kV Ar^+, $\sim 5\ \mu$A for 15 mins) and annealing at 800 K (1 min). The base pressure in the scattering chamber was $< 3 \times 10^{-11}$ mbar, and the surface quality was monitored using helium reflectivity measurements. The high specular reflectivity of the sample to helium ($\sim 20\%$), together with the sharp peaks seen in diffraction patterns of the clean surface (Fig. 1), allow us to estimate that the adsorbate and vacancy concentrations of the surface are $<1\%$ [24]. Our measurements of the low energy, low intensity phason modes were enabled by the recent addition to the apparatus of a detector with improved sensitivity [25], and were made at a sample temperature of 200 K.

Large scale molecular dynamics simulations of the Au(111) reconstruction [26,27], based on the nonlinear double-sine-Gordon (DSG) potential model [28], have previously been used to reproduce the experimentally observed structural features described above, including the herringbone structure. In this model, PMD pairs appear as a DSG soliton (bound pairs of sine-Gordon solitons). The dynamical simulation results provide an excellent fit to surface phonon dispersion curves measured by inelastic helium atom scattering [19]. They also revealed two types of low-lying dispersive branches associated with the lattice of DSG solitons: an inter-DSG excitation branch, which we label an acoustic phason, and an intra-DSG branch arising from the internal low-energy dynamical mode of the bound pair [29,30], designated an optical phason. This mode assignment naturally arises when we consider the apparent

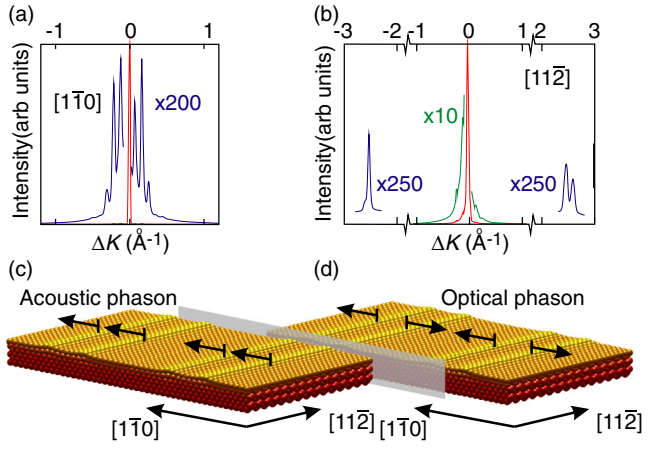

FIG. 1 (color online). The DSG soliton reconstruction of the Au(111) surface. (a) and (b) show helium diffraction scans of the clean Au(111) surface along the $\langle 1\bar{1}0\rangle$ and $\langle 11\bar{2}\rangle$ directions, respectively. (c) and (d) are schematic representations of the Au(111) surface with arrows showing the relative motion of atoms in each DSG topological soliton at the zone center for the acoustic and optical phason modes, respectively.

analogy between the DSG lattice configuration and a lattice of diatomic molecules. The excitations are referred to as phasons due to the fact that the positions of the soliton constituent atoms are set in terms of well defined relative phases. Thus, the excitations involve precise changes in these phases to produce the infinitesimal displacive motion of the solitons. For mathematical and other details, see the Supplemental Material [31].

Figures 1(a) and 1(b) show diffraction scans of the Au(111) surface along the $\langle 1\bar{1}0\rangle$ and $\langle 11\bar{2}\rangle$ directions showing good agreement with the results of Harten *et al.* [16] and confirming the presence of the $23 \times \sqrt{3}$ reconstruction on the clean Au(111) surface. Figures 1(c) and 1(d) are schematic representations of the Au(111) surface capturing the essential features of the DSG model representation, each showing the periodic lattice of PMD pairs with two DSG solitons. The surface topography is indicated by the shading of the atoms, with higher atoms highlighted. The relative motion of atoms in each DSG topological soliton at the zone center is shown with arrows for displacements of the acoustic and optical phason modes, and it is the dispersion of these modes along the $\langle 1\bar{1}0\rangle$ direction that we have determined in the present work.

Figure 2 shows three energy transfer spectra identifying elastic and inelastic events on the scattering of helium from the Au(111) surface. Data points are shown as black circles, and the thick black line delineating the data in each spectrum is found from the sum of the constituent peaks. A quasielastic helium atom scattering (QHAS) peak is seen at $\Delta E = 0$, with the peak width reflecting the intrinsic energy resolution of the method. Peaks appearing closer to the QHAS peak than the surface Rayleigh phonon peaks (green) are identified as phason modes, with the acoustic and optical phason modes highlighted in red and blue respectively. Mode assignments were initially made on the basis of the peak position in energy, and then used to determine the phason dispersion with $\Delta\mathbf{K} \equiv \mathbf{q}$, the phason wave vector, as shown in Fig. 3(a). The vertical dashed lines in Fig. 2 give the predicted positions of the phason modes determined by the dynamical model (discussed below and in Ref. [31]), which correspond well to the peak positions, demonstrating the self-consistency of this approach.

In Fig. 3(a), we plot the peak positions from a number of energy transfer spectra as a function of ($\Delta\mathbf{K}$, ΔE). Phason and phonon events identified from the spectra typified by Fig. 2 appear as blue asterisks with the corresponding peak widths represented by thick blue lines. These lines fall along dashed black scan lines that represent constrained functions of ($\Delta\mathbf{K}$, ΔE) defined by the beam energy and scattering geometry. Note that for clarity Fig. 3(a) focuses on data points in the energy range of $\Delta E < 0.55$ meV, corresponding to the phason modes. Figure 3(a) also allows us to understand the broadening of the inelastic peaks seen in Fig. 2. A sharp

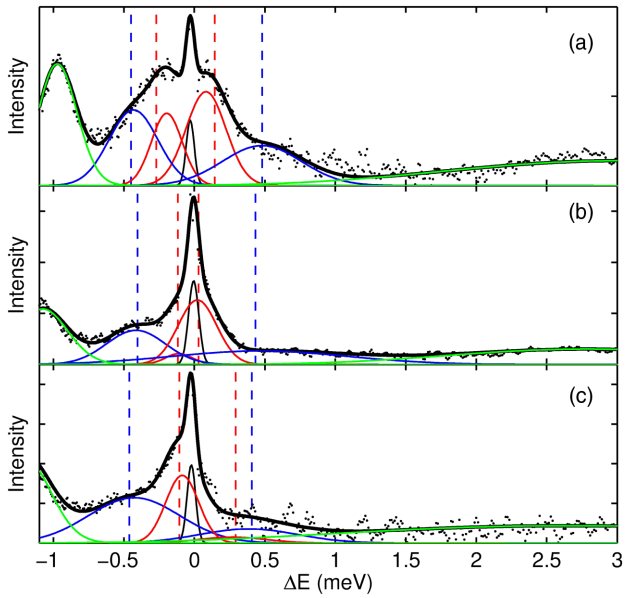

FIG. 2 (color online). A series of three one-dimensional phonon spectra for (a) $\theta_i = 19.825°$, (b) $\theta_i = 19.575°$, and (c) $\theta_i = 19.325°$ along $\langle 1\bar{1}0 \rangle$. Data points are shown in black, with the sum of the fits to the data shown with a thick solid black line. Peaks identified to make up the total fit are highlighted with thin lines, with Rayleigh modes (green), acoustic phason modes (red), optical phason modes (blue) and a QHAS peak (black). The vertical dashed lines show the position of the phason peaks predicted by the dispersion curve from the dynamical model with parameters which best describe the complete data set.

intersection of a black scan line with the mode dispersion yields a sharp peak, while an oblique intersection gives a broad peak. More formally, this broadening arises from the projection of inelastic features in the two-dimensional matrix relating the incident and scattered energies of the helium beam onto a one-dimensional axis [21,22], such that the elastic features appear with their true widths, while the apparent width of the inelastic peaks depends on the spin-echo scanning parameters employed. Data obtained at higher values of ΔE depicting Rayleigh and longitudinal surface phonon events are shown in Fig. S2 of the Supplemental Material [31] and are in good agreement with the earlier results of Harten *et al.* [19]. The acoustic and optical phason mode dispersions are consistent with the results of earlier molecular dynamics simulations [26,27]. Figure 3(b) shows the same data as Fig. 3(a), but in a reduced zone representation, with all data points moved into the first Brillouin zone. Further energy transfer spectra used to construct Figs. 3(b) and 3(b) are presented and peak broadening is discussed in more detail in the Supplemental Material [31].

The phason dispersion curves shown in red in Figs. 3(a) and 3(b) are the best fit results to the data obtained by modeling the dynamics of the lattice of partial dislocations as composed of sine-Gordon solitons

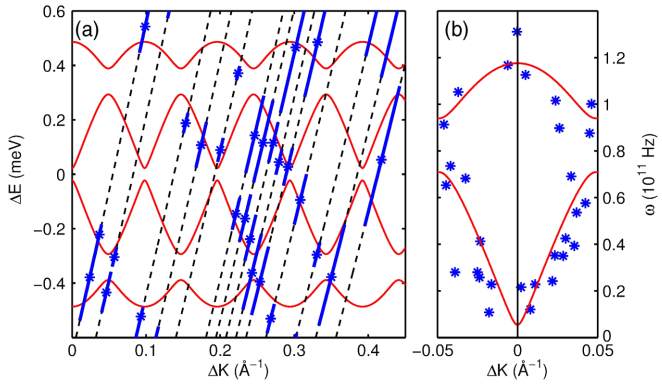

FIG. 3 (color online). Phonon and phason dispersion curves for the clean Au(111) surface. (a) Extended zone representation. Data points are shown in blue, with thick blue lines representing the corresponding peak width. Data points fall along scan curves $\Delta E(\Delta \mathbf{K})$, shown with black dashed lines. Red curves show the best-fit acoustic and optical phason mode dispersion relations. (b) Reduced zone representation, with all data points moved to lie in the first Brillouin zone, showing good agreement between data (blue asterisks) and the best-fit dispersion curves (red).

with alternating spring constants. This yields frequencies of 275 μeV for the internal mode, 206 μeV for the inter-DSG vibration mode, and 45 μeV for the pinning potential. Note that the bandwidth of the acoustic branch [lower curve in Fig. 3(b)] is wider than that of the optical one (upper curve). The effective force constants can also be obtained assuming a dislocation partial effective mass of approximately $M = 10 M_{\mathrm{Au}}$, and we find the DSG internal constant $\alpha = 15.3 \times 10^{-3}\ \mathrm{N\,m^{-1}}$, the inter-DSG constant $\beta = 8.7 \times 10^{-3}\ \mathrm{N\,m^{-1}}$, and the dislocation pinning constant $\gamma = 1 \times 10^{-4}\ \mathrm{N\,m^{-1}}$. Full mathematical details are given in the Supplemental Material [31].

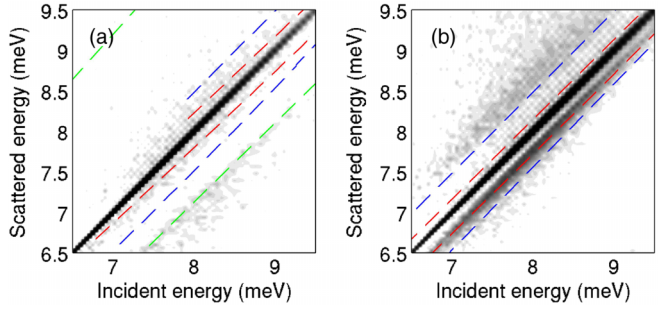

FIG. 4 (color online). 2D measurement showing the measured spectral intensity as a function of the incident and scattered energies for (a) $\theta_i = 19.6°$ and (b) $\theta_i = 21.6°$. The nonlinear gray scale is chosen to emphasize the spectral features, ranging from white (lowest intensity) to black (maximum intensity). The expected positions of the Rayleigh phonon (green), acoustic phason modes (red) and optical phason modes (blue) are shown with dashed lines.

Confirmation of the data deduced from the one-dimensional spectra (Fig. 2) is provided by 2D measurements of the scattered energy as a function of incident energy, employing compressed sensing methods [23,32]. Figure 4 shows typical results, for (a) $\theta_i = 19.6°$ and (b) $\theta_i = 21.6°$, with each panel giving the spectral intensity of the matrix relating the incident and scattered beam energies on a gray scale. The elastic peak appears as a high intensity (black) diagonal feature stretching from the bottom left to top right of the figure. Features lying below this elastic line represent energy-loss events, and those above the elastic line energy-gain events. The position of the Rayleigh phonon mode from the results of Harten *et al.* [19] is shown in green, and the positions of the acoustic and optical phason modes predicted by the dynamical model describing the data are shown in red and blue, respectively. In Fig. 4(a), for an incident angle $\theta_i = 19.6°$ the Rayleigh mode and acoustic phason intensity are clearly seen, although the optical mode is not distinguishable due to its low spectral intensity. In contrast Fig. 4(b), with a different accessible range of ($\Delta\mathbf{K}$, ΔE) as determined by the different scattering geometry, shows both the optical and acoustic phason modes clearly. Note the accepted convention that the oscillator strength of the Rayleigh mode for $\Delta E < 0.8$ meV is transferred to the soliton modes, which was confirmed for this system by the previous molecular dynamics simulations [26,27]. These results are also presented as a series of 1D spectra in the Supplemental Material [31]. Finally, note that by construction, 2D measurements as in Fig. 4 show the position and width of the inelastic intensity faithfully, and hence provide further evidence for the presence and dispersion of the phason modes.

In summary, we have observed phason modes arising from the lattice of PMDs on the Au(111) surface and have, for the first time, determined the dispersion of their acoustic and optical phason branches along with quantitative information about the energetics of the domain structure in the reconstruction. Our results agree well with earlier predictions from molecular dynamics simulations [29,30]. Additionally, we have demonstrated the power of HeSE in resolving very low energy vibrational modes close to the specular signal, where conventional vibrational spectroscopy methods fail. The 2D measurement enabled direct observation of the optical phason mode despite its low-lying dispersion, indicating the potential of HeSE with sparse sampling methods for future studies of low energy vibrational excitations. As *ab initio* methods increase in sophistication, the modeling of complex structures such as partial misfit dislocations should be possible, and the present work provides direct experimental evidence to underpin such calculations.

M. E.-B. is supported by the U.S. Department of Energy under Grant No. DE-FG02-85ER45222. All other authors acknowledge financial support from the EPSRC.

*emb56@cam.ac.uk
†elbat@bu.edu

[1] V. Bulatov, L. Hsiung, M. Tang, A. Arsenlis, M. Bartelt, W. Cai, J. Florando, M. Hiratani, M. Rhee, G. Hommes, T. Pierce, and T. de la Rubia, Nature (London) **440**, 1174 (2006).
[2] K. Thurmer, R. Hwang, and N. Bartelt, Science **311**, 1272 (2006).
[3] Y. I. Frenkel and T. Kontorova, Zh. Eksp. Teor. Fiz. **8**, 1340 (1938).
[4] F. Frank and J. van der Merwe, Proc. R. Soc. A **198**, 205 (1949).
[5] F. Frank and J. van der Merwe, Proc. R. Soc. A **198**, 216 (1949).
[6] F. Nabarro, *Theory of Crystal Dislocations* (Clarendon, Oxford, 1967).
[7] J. Evans, P. Thiel, and M. Bartelt, Surf. Sci. Rep. **61**, 1 (2006).
[8] A. K. Schmid, N. C. Bartelt, J. C. Hamilton, C. B. Carter, and R. Q. Hwang, Phys. Rev. Lett. **78**, 3507 (1997).
[9] J. de la Figuera, K. Pohl, O. R. de la Fuente, A. K. Schmid, N. C. Bartelt, C. B. Carter, and R. Q. Hwang, Phys. Rev. Lett. **86**, 3819 (2001).
[10] M. van Hove, R. Koestner, P. Stair, J. Bibrian, L. Kesmodel, I. Barto, and G. Somorjai, Surf. Sci. **103**, 189 (1981).
[11] J. Heyraud and J. Metois, Surf. Sci. **100**, 519 (1980).
[12] C. Wöll, S. Chiang, R. J. Wilson, and P. H. Lippel, Phys. Rev. B **39**, 7988 (1989).
[13] J. V. Barth, H. Brune, G. Ertl, and R. J. Behm, Phys. Rev. B **42**, 9307 (1990).
[14] A. R. Sandy, S. G. J. Mochrie, D. M. Zehner, K. G. Huang, and D. Gibbs, Phys. Rev. B **43**, 4667 (1991).
[15] K. Takayanagi and K. Yagi, Trans. Jpn. Inst. Met. **24**, 337 (1983).
[16] U. Harten, A. M. Lahee, J. P. Toennies, and C. Wöll, Phys. Rev. Lett. **54**, 2619 (1985).
[17] S. M. Driver, T. Zhang, and D. A. King, Angew. Chem., Int. Ed. Engl. **46**, 700 (2007).
[18] A. Jardine, H. Hedgeland, G. Alexandrowicz, W. Allison, and J. Ellis, Prog. Surf. Sci. **84**, 323 (2009).
[19] U. Harten, J. P. Toennies, and C. Wöll, Faraday Discuss. Chem. Soc. **80**, 137 (1985).
[20] F. Hofmann and J. Toennies, Chem. Rev. **96**, 1307 (1996).
[21] G. Alexandrowicz and A. P. Jardine, J. Phys. Condens. Matter **19**, 305001 (2007).
[22] P. R. Kole, A. P. Jardine, H. Hedgeland, and G. Alexandrowicz, J. Phys. Condens. Matter **22**, 304018 (2010).
[23] M. Lustig, D. L. Donoho, J. M. Santos, and J. M. Pauly, Stanford University, Report No. 2007-3, 2007.
[24] B. Poelsema and G. Comsa, *Scattering of Thermal Energy Atoms from Disordered Surfaces* (Springer, New York. 1989).
[25] D. Chisnall, Ph.D. thesis, University of Cambridge, 2012.
[26] R. Ravelo and M. El-Batanouny, Phys. Rev. B **40**, 9574 (1989).
[27] R. Ravelo and M. El-Batanouny, Phys. Rev. B **47**, 12 771 (1993).

[28] M. El-Batanouny, S. Burdick, K. M. Martini, and P. Stancioff, Phys. Rev. Lett. **58**, 2762 (1987).
[29] P. Sodano, M. El-Batanouny, and C. R. Willis, Phys. Rev. B **34**, 4936 (1986).
[30] S. Burdick, M. El-Batanouny, and C. R. Willis, Phys. Rev. B **34**, 6575 (1986).
[31] See Supplemental Material at http://link.aps.org/supplemental/10.1103/PhysRevLett.110.086103 for additional experimental data and further background to the experimental technique and DSG solitons.
[32] R. Bell, P. R. Kole, D. J. Ward, J. Ellis, and W. Allison (to be published).